Journal of Manufacturing Processes 167 (2026) 289–304

Contents lists available at ScienceDirect

Journal of Manufacturing Processes

journal homepage: www.elsevier.com/locate/manpro

A hybrid mesh-based framework for accurate and convenient macro-shape prediction of cold spray deposits

Mohammad Reza Mehraban, Mario Guagliano, Sara Bagherifard [*]

Politecnico di Milano, Department of Mechanical Engineering, Milan, Italy

HIGHLIGHTS

- A two-phase modeling framework is proposed for cold spray deposit shape prediction.
- Shape parameters are derived from only one single experimental deposition profile.
- A mesh-based simulator predicts complex deposits with high fidelity.
- The model predictions show strong agreement with copper and Ti6Al4V experiments.
- The approach reduces experimental demand while improving prediction accuracy.

ARTICLE INFO

Keywords:
Cold spray
Deposition shape prediction
Shadow effect
Geometrical accuracy

ABSTRACT

Accurate prediction of deposition geometry is essential for achieving dimensional control in cold spray additive manufacturing, repair and welding. Various approaches have been lately implemented to address this gap. However, there is still considerable space for improvement as the existing analytical and numerical models either lack generalizability or incur high computational costs, while most machine learning methods commonly require large experimental datasets and often disregard underlying physics. This study presents an efficient computational framework to overcome these limitations. First, a numerical approach is developed to conveniently extract the empirical parameters of the analytical shape-estimating model using only a single experimental deposition profile. This approach enables the derivation of the deposit shape parameters and the relative deposition efficiency as a function of impact angle. In the second phase, a mesh-based simulator is introduced, incorporating these parameters along with an enhanced shadowing algorithm tailored for thick and complex depositions. The robustness of the parameter extraction method is validated through a parametric study, and the predictive capability of the model is verified against experimental data for pure copper and titanium alloy Ti6Al4V under various spraying conditions. Moreover, various demonstrations highlight the utility of the predictive model for potential toolpath planning to control the deposition shape. The proposed framework enables accurate simulation of the deposition profiles with minimum experimental input, offering an efficient and physically consistent tool for cold spray deposit shape prediction and control.

1. Introduction

As an emerging deposition technique, cold spray (CS) has been employed to deposit a wide range of materials, including metals, composites, cermets, metallic glasses, and high-entropy alloys [1–4]. The solid-state deposition feature distinguishes the CS process among thermal spraying techniques, preventing metal melting. This characteristic is shared with other advanced manufacturing or joining techniques like friction stir welding and binder jetting, and critically enables the formation of joints and deposits that are free from solidification defects such as hot cracks typically associated with fusion-based technologies [5–7]. Consequently, this CS feature makes it capable of thick deposition with low porosity and minimum residual stresses [8]. These advantages have expanded CS applications beyond coatings to include additive manufacturing (AM), repair, and welding [9–12]. In such applications, geometrical control of material buildup is as crucial as achieving desirable structural properties. Nevertheless, the spraying nature of CS processes imposes significant limitations on geometrical accuracy and

---

* Corresponding author.
E-mail addresses: mohammadreza.mehrabankoopaei@polimi.it, Rezamehraban940@gmail.com (M.R. Mehraban), sara.bagherifard@polimi.it (S. Bagherifard).

https://doi.org/10.1016/j.jmapro.2026.03.070
Received 5 October 2025; Received in revised form 26 February 2026; Accepted 28 March 2026
Available online 3 April 2026
1526-6125/© 2026 The Author(s). Published by Elsevier Ltd on behalf of The Society of Manufacturing Engineers. This is an open access article under the CC BY license (http://creativecommons.org/licenses/by/4.0/).

the possibility of obtaining uniform deposition profiles [13,14]. Currently, iterative approaches are predominantly used for controlling the deposit shape. Therefore, expanding the applicability of CS within industrial contexts necessitates the advancement of shape predictive methodologies across varying toolpaths, process parameters, and material selections.

Early efforts in CS deposition prediction began with Cai et al. [15], who leveraged the Gaussian shape of a single track profile to define Gaussian curves to fit experimental data of track profiles at different stand-off distances (SoD), estimating coating thickness through curve superposition. A similar approach was later adapted to incorporate the effects of spraying angle [16], nozzle speed [16], and non-planar substrates [17,18]. However, despite the interesting results, the models could not account for the obstructive effect, known as the "*shadow effect*", that occurs on non-convex surfaces, preventing material deposition in certain areas. Capturing the shadow effect is indeed crucial for accurate predictions in multi-layer AM applications. A numerical solution featuring an algorithm for detecting surface obstructions was suggested by Wu et al. [19] to address this issue. This model represents the particle jet with a divergent conical shape to capture the behavior of the gas stream more accurately. Nonetheless, the new model can become computationally intensive when aiming for smooth and accurate simulations, as its performance depends on the number of cylindrical rays used to discretize the particle jet. It also only considers the spraying angle on the initial surface, which may result in a loss of accuracy as the deposition grows [13]. An FE model exhibiting similar deficiencies was also developed later by Li et al. [20].

Around the same time, to leverage the physical phenomenon of spraying, Klinkov et al. [21,22] proposed a new analytical model that describes the deposition growth rate over time and space using a partial differential equation (PDE). The PDE determines the deposition at a given point and a time interval based on the deposition profile and the relative deposition efficiency (DE) associated with the impact angle, which is defined as the angle between the substrate normal and the nozzle axis. This model suits complex and thick CS processes, encountered especially in AM applications, as it incrementally updates the geometry during spraying. Subsequently, Vanerio et al. [23] developed a 3D mesh-based program that integrates an updated Klinkov's approach with the shadow effect algorithm developed in [19]. The proposed model adds flexibility in terms of nozzle trajectory and substrate geometry. Its ability to account for various process parameters was experimentally validated, exhibiting robustness also in the case of non-planar substrates (e.g., repair and welding), superimposed tracks and non-Gaussian particle jet distribution profile. Although this model showed great potential for various applications [24], it was limited to simulating a single track at a time and did not fully consider nozzle divergence effects by varying SoD, which are important for realistic additive build scenarios. Recently, Xing et al. [25] developed a computational fluid dynamics-integrated, layer-stacking method for 3D profile prediction in CS additive manufacturing, incorporating a critical velocity criterion to regulate DE. While their model achieves high accuracy and requires no experimental input, it involves high computational costs. Additionally, it remains unclear how the model accounts for the shadow effect, which can significantly influence deposition outcomes in multi-layer and complex geometries.

Alternatively, machine learning (ML) models have been more recently leveraged to predict CS deposition shape without the need to define explicit equations. Instead, they are trained directly using experimental [26–28], numerical [29], or combined data [30]. Mostly based on neural networks, these models are able to flexibly capture complex behaviors [13]. In addition, when trained with empirical data, they can implicitly account for subtle effects that are often overlooked or simplified in analytical models. Nevertheless, to achieve adequate generalization, ML requires large datasets and retraining for each material system. Physics-guided ML models offer a potential middle ground by embedding physical insights to reduce data needs [29,30]. Still, further development is needed to improve their reliability, especially for multi-layer, thick depositions typical of CS additive manufacturing [29]. Comprehensive details on the various ML-based methods used to simulate deposition shape are given in [29].

All the aforementioned predictive approaches require calibration using experimental data. In analytical models, this is done by defining material- and process-dependent constants, while in ML models, calibration occurs implicitly through training. For instance, Klinkov's model [21,22] incorporates two distinct parameters characterizing the deposition shape, as well as a functional expression for the impact angle dependence, each of which typically necessitates multiple experimental runs for accurate determination. To calibrate the parameters and the impact-angle-dependent function, two main methods exist: trial-and-error comparison of simulations with experiments [23], and direct measurements (e.g., weighing samples before and after spraying, especially applicable for impact angle effects) [19]. Typically, seven or eight experimental deposition profiles (two or three for shape-dependent parameters and four or five for the angle-dependent function) are utilized to calibrate the analytical model using these approaches. This makes the predictions relatively time-consuming and costly. Moreover, when the thickness of the deposited layer produced by inclined spraying exceeds relatively thin profiles, the assumption that the measured DE corresponds to the initial substrate angle becomes invalid.

To systematically address these challenges and reduce the experimental effort needed for model calibration and shape prediction, this study introduces a numerical framework structured in two main parts. First, we introduce a numerical approach designed to extract the key features of the analytical model, namely, the parameters governing deposition shape and the DE as a function of impact angle, using just one experimental test. This model is then validated using experimental profiles obtained from deposits with various pass numbers. Its results are then passed to the second phase for simulation, where a new mesh-based solver for the analytical model is proposed, which addresses the limitations of the earlier models, especially regarding the integration of a new shadowing effect algorithm. Finally, a comparison with experimental data and other computational methods is performed to demonstrate the accuracy of the output of the developed framework.

The specific technical objectives of this research are:

- To significantly reduce the experimental burden for model calibration by precisely determining all material- and process-dependent analytical constants from a single deposition profile.
- To implement a physically accurate deposition model by incorporating advancements such as a divergent particle jet and calculating growth along the surface normal.
- To ensure high geometrical fidelity for complex and thick structures through a novel, mesh-independent shadowing algorithm.
- To develop a framework with the flexibility to simulate arbitrary toolpaths and nozzle orientations for efficient toolpath planning and macro-shape control in AM and repair applications.

2. Analytical fundamentals

In this section, we present a brief overview of the analytical foundations of Klinkov's model, which forms the basis of the subsequent numerical model. We also delineate the enhancements introduced to improve the model's fidelity to physical phenomena.

These modifications include introducing a relative DE to capture the effects of SoD, as proposed in [23], and scaling the deposition shape at different SoDs to maintain consistent mass deposition while accounting for a divergent particle jet.

Klinkov's 3D model defines the growth rate ($\frac{\partial Z}{\partial t}$) as a function of distance to the nozzle axis (r) and the impact angle (α) as follows [22]:

$$\frac{\partial Z}{\partial t} = A \cdot DE(\alpha) \cdot J(r) \tag{1}$$

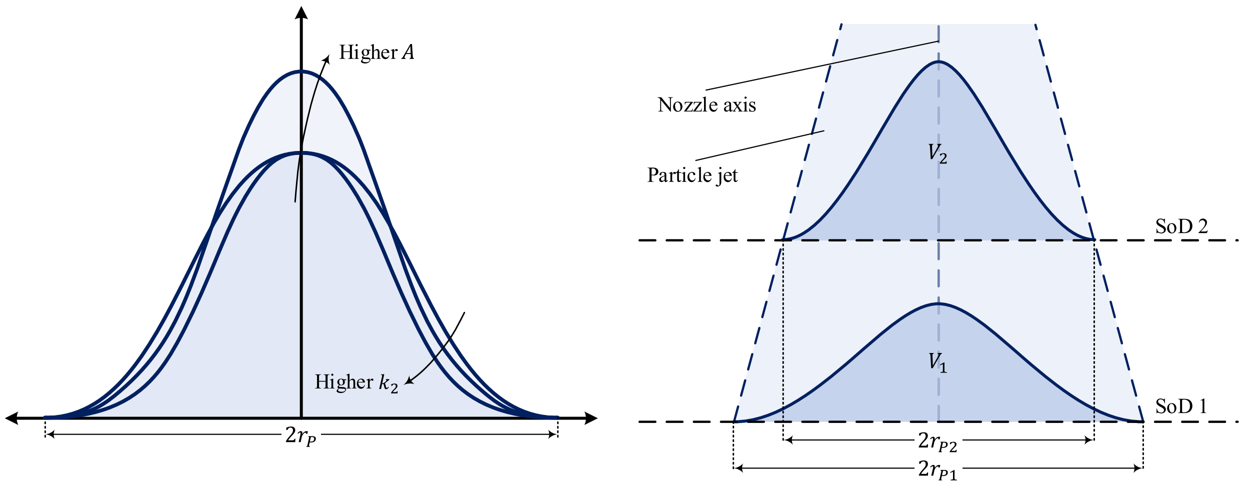

(a) (b)

Fig. 1. (a) Schematic of single-track deposition cross-section illustrating the effect of analytical model's main parameters on the profile. (b) Scaling the deposition shape with respect to the SoD while maintaining a constant deposition volume.

In Eq. (1), A is a constant that determines the deposition rate and depends on the process parameters, such as the powder feed rate, nozzle speed, etc. $DE(\alpha)$ represents the relative DE as a function of the impact angle, α, and $J(r)$ is the particle distribution. $DE(\alpha)$ equals 1 when the nozzle axis is perpendicular to the substrate and gradually decreases to zero as the angle between the nozzle axis and the substrate approaches a critical limit, denoted by α_m [22].

It is assumed that particles travel parallel to the nozzle axis, with the majority remaining closer to the nozzle axis. This assumption has been validated by empirical observations, making an axisymmetric distribution an effective way to describe the deposition shape based on a point's distance from the nozzle axis, when using axisymmetric nozzles of circular profile [22]. Although this may not hold for all powders and particle size distributions [23], a Gaussian-based function is widely accepted for expressing the particle distribution $J(r)$ as shown in Eq. (2) [24].

$$J(r) = \begin{cases} \dfrac{\exp\left(-k_2\left(\frac{r}{r_P}\right)^2\right) - \exp(-k_2)}{1 - \exp(-k_2)}, & r \leq r_P \\ 0, & r > r_P \end{cases} \tag{2}$$

In the above equation, r_P determines the boundary of the spraying area, while k_2 defines the steepness of the deposition shape. A higher k_2 results in more concentrated particle jets, whereas lower k_2 values lead to more uniform distributions. Moreover, a mathematical relation for $DE(\alpha)$ is derived by fitting a curve to experimental tracks obtained for several nozzle inclination angles. It should be noted that all the parameters, i.e., A, k_2, r_P, and $DE(\alpha)$, are commonly determined experimentally and vary depending on the material system and CS process parameters. Fig. 1a schematically illustrates the effects of A and k_2 on the cross-section profile of the deposition shape.

Klinkov's model [21,22] assumes that particles travel parallel to the nozzle axis, implying a cylindrical gas stream shape. However, since the exiting gas pressure is higher than the ambient pressure, the stream continues to expand after leaving the De Laval nozzle [31,32]. This assumption has been supported by experimental observations where the deposition width is always larger than the nozzle diameter and increases as the SoD grows (see Fig. 1b). To account for these effects, we scaled the deposition profile accordingly using a mass conservation approach. Assuming a constant k_2 and feed rate, the new deposition profile for a different SoD can be derived from a reference SoD as follows

$$A\cdot\int_0^{2\pi}\int_0^{r_P} J(r, r_P(SoD))\,dr\,d\pi = A^{ref}\cdot\int_0^{2\pi}\int_0^{r_P^{ref}} J\left(r, r_P^{ref}\right)dr\,d\pi \tag{3}$$

After performing the integration and simplifying the expression, the final equation is described as:

$$A = A^{ref}\cdot\frac{r_P^{ref}}{r_P(SoD)} \tag{4}$$

In addition, SoD can affect the DE. When SoD exceeds an upper bound critical threshold or falls below a lower bound critical threshold, the particles either fail to acquire sufficient kinetic energy for proper adhesion or begin to lose the requisite momentum for effective deposition onto the substrate before reaching it [19]. Generally, the function $DE(SoD)$ is derived by fitting a polynomial to the experimental results. By adding the mathematical expression of the mentioned considerations to Eq. (1), it can be rewritten as follows:

$$\frac{\partial}{\partial t}(Z_{n_s}(t, SoD, r, \alpha)) = A(SoD, t)\cdot DE(\alpha, t)\cdot J(r, SoD, t)\cdot DE(SoD, t) \tag{5}$$

where Z_{n_s} represents the surface normal at a given point and time.

By selecting a specific SoD as the reference value, and measuring the resulting deposition width, i.e., $2r_P^{ref}$, the divergence ratio of the particle jet can easily be calculated. The deposition width, $2r_P$, at any other SoDs can then be determined using simple geometrical relations. On the other hand, $DE(SoD)$ remains close to 1 when the SoD is kept within an optimal range, which is typically maintained during spraying. Therefore, the most influential parameters on the deposit profile are A^{ref}, k_2, and $DE(\alpha)$.

3. Numerical framework

The following subsections provide details of the numerical model used to solve Eq. (1) over a general spatial and temporal domain. As mentioned, the prerequisite to solving Eq. (1) is the proper determination of empirical constants, which are usually derived from multiple experimental tests for each material and CS process parameters. In this section, we first describe a systematic numerical approach developed to determine these constants using only one single experimental deposition profile. Subsequently, we outline the second phase, which is a mesh-based model developed to simulate the CS deposit shape formation.

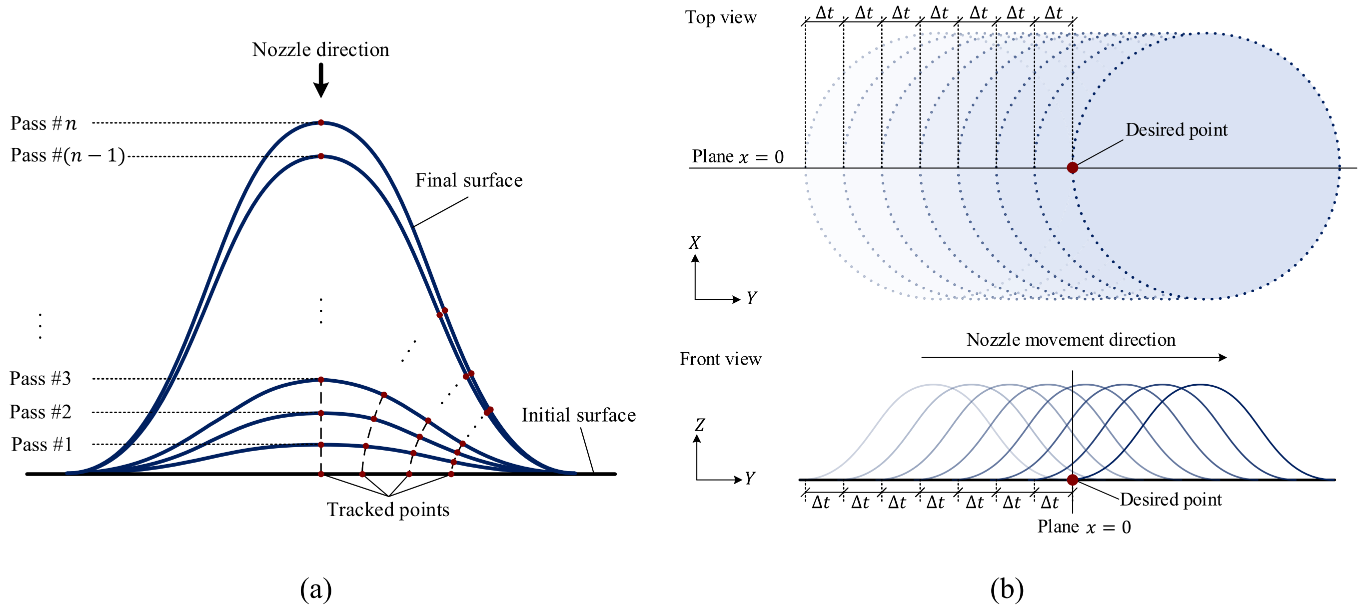

(a)

(b)

Fig. 2. (a) Schematic illustration of the methodology developed for extracting empirical constants from a single experimental profile. (b) The discretization of the time during which a point at $x = 0$ is subjected to the influence of a transversing nozzle.

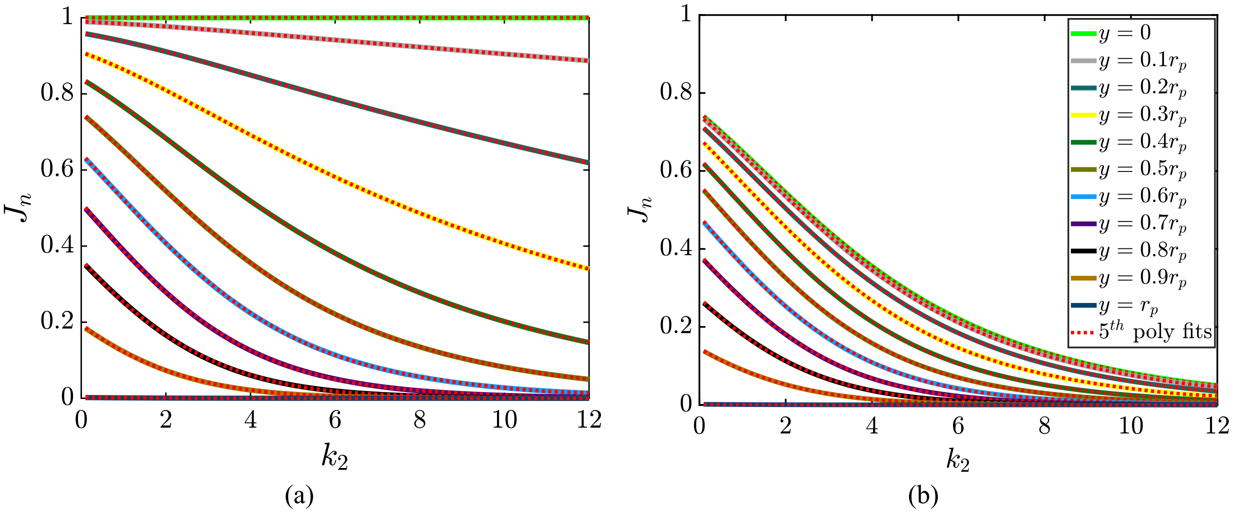

(a)

(b)

Fig. 3. Representative J_n curves and the corresponding 5th-order polynomial fits at (a) $x = 0$, (b) $x = 0.5r_p$.

3.1. Phase I: analytical model's constant extraction

The notion underlying extracting empirical constants from a single experimental test is shown in Fig. 2a. By tracking surface points after each spray pass, we observe that as the material accumulates layer by layer, each point experiences different impact angles over time. In addition, the final shape of deposition is a result of the superimposition of several deposition profiles. Hence, considering the evolution of what individual points are experiencing as the deposit grows, all the necessary information can be extracted from a single experimental profile. Here we propose an effective method to extract this information.

Herein, a single-track deposition refers to material deposited by nozzle movement along the y-axis (refer to Fig. 2b) at a constant transverse speed of v_s. Each single track may contain multiple nozzle passes on the same trajectory. In addition, we assume the cross-sectional profile of the deposits remains constant along the spraying direction, i.e., y-axis, apart from its extremities.

Since extracting empirical constants from a single-track deposition profile is an inverse problem, incorporating physical insights is essential to constrain the solution space and ensure realistic and meaningful output. To do that, we first consider a point located at $x = 0$ in a spraying process, where the highest amount of deposition occurs. Due to the shape of the particle jet, it is reasonable to assume that in a single-track deposition, where the nozzle axis stays perpendicular to the substrate, the impact angle at points located at $x = 0$ always remains 90°. It should be noted that this assumption remains valid only as long as the deposit shape is symmetric and the peak does not exhibit a significant slope. Consequently, the experimental input for this code should be obtained from a multi-pass deposition on a flat substrate. While the number of passes must be sufficient to extract $DE(\alpha)$ at high impact angles, the resulting peak should remain smooth enough to ensure that the underlying assumption continues to hold. Also, assuming the given SoD as the reference, Eq. (5) can be simplified as follows:

$$\left.\frac{dZ_{n_s}}{dt}\right|_{x=0} = A^{ref}\cdot J\left(r(t), r_P^{ref}\right) \tag{6}$$

Table 1
Polynomial coefficients computed for different points along the deposition profile.

Point position	$x = 0$	$x = 0.25r_p$	$x = 0.5r_p$	$x = 0.75r_p$
C_5^*	1.37×10^{-6}	1.65×10^{-6}	2.24×10^{-6}	9.56×10^{-6}
C_4^*	-4.49×10^{-5}	-5.50×10^{-5}	-7.07×10^{-5}	-1.75×10^{-5}
C_3^*	4.53×10^{-4}	5.79×10^{-4}	6.44×10^{-4}	-1.74×10^{-4}
C_2^*	1.49×10^{-4}	-2.20×10^{-4}	1.32×10^{-3}	6.28×10^{-3}
C_1^*	-3.50×10^{-2}	-4.08×10^{-2}	-5.31×10^{-2}	-5.22×10^{-2}
C_0^*	0.33	0.31	0.25	0.15
Average R^2	1.0000	1.0000	1.0000	1.0000

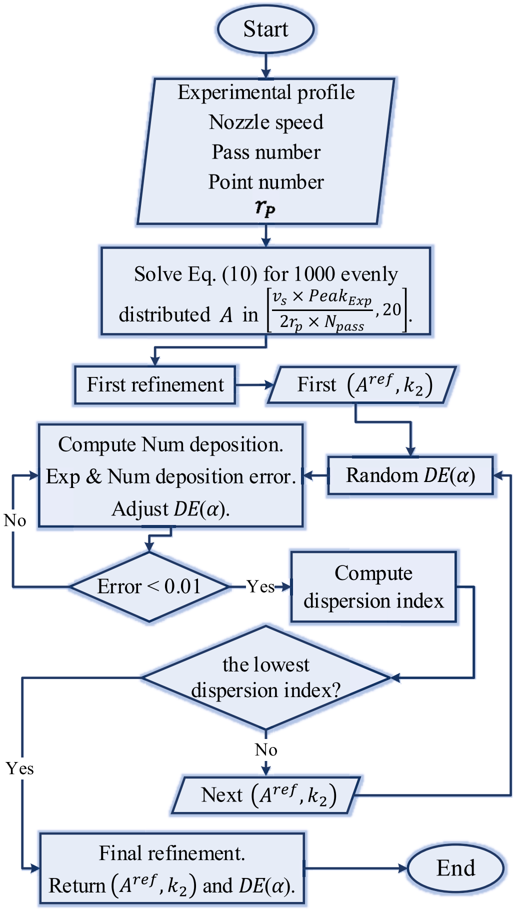

Fig. 4. Flowchart of the algorithm developed for extracting empirical parameters of Eq. (5).

As seen in Eq. (6), the equation no longer depends on spatial variables and has been reduced to an ordinary differential equation (ODE). In addition, the total time during which a point at $x = 0$ is influenced by the nozzle is $\frac{2r_P^{ref}}{v_s}$. This represents the time, starting from when the nozzle starts to pass over the point until it has fully moved past it (see Fig. 2b). Now, if we split this time into M small intervals, Eq. (6) can be stated as follows:

$$\Delta Z_{n_s}\big|_{x=0} = A^{ref} \sum_{n=1}^{M} \Delta t_n J_n\left(r_n, r_P^{ref}\right) \tag{7}$$

Considering the symmetry of the deposition shape, the number of passes, and expressing r_n in terms of Δt, the total deposition height at a point at $x = 0$ can be estimated by:

$$\Delta Z_{n_s}\big|_{x=0} = 2N_{pass}.\Delta t.A^{ref} \sum_{n=0}^{\frac{M-1}{2}} J_n\left(n\Delta t, r_P^{ref}\right) \tag{8}$$

The right-hand side of Eq. (8) represents the final deposition height after N_{pass} passes, which is known. However, A^{ref} and J_n are unknown, with J_n being a function of k_2. Moreover, the shape of J_n, Eq. (2), is not convenient for numerical solutions. To overcome these issues, first, a reasonable range is considered for k_2, from 0.1 to 12, and a 5th-order polynomial is fitted to each J_n. Fig. 3 illustrates the J_n curves and the corresponding 5th-order polynomial fits (red dotted lines) as a function of k_2 for $M = 21$.

Substituting the new polynomial expressions for J_n into Eq. (8), gives

$$\Delta Z_{n_s}\big|_{x=0} = 2N_{pass}A^{ref}.\frac{2r_P^{ref}}{v_s}.\frac{1}{M}\sum_{n=0}^{\frac{M-1}{2}}\left[C_{5,n}k_2^5 + C_{4,n}k_2^4 + C_{3,n}k_2^3 + C_{2,n}k_2^2 + C_{1,n}k_2 + C_{0,n}\right] \tag{9}$$

For a given M, the sum of the polynomial coefficients can be computed directly, simplifying the evaluation of the total deposition height at specific points, as listed in Table 1. Note that M must be an odd integer and sufficiently large to ensure that the sum of the polynomial coefficients converges.

The final form of the Eq. (9) is

$$\Delta Z_{n_s}\big|_{x=0} = 2N_{pass}A^{ref}\frac{2r_P^{ref}}{v_s}\left[C_5^*k_2^5 + C_4^*k_2^4 + C_3^*k_2^3 + C_2^*k_2^2 + C_1^*k_2 + C_0^*\right] \tag{10}$$

with $C_5^* = \frac{1}{M}\sum C_{5,n}$, $C_4^* = \frac{1}{M}\sum C_{4,n}$, $C_3^* = \frac{1}{M}\sum C_{3,n}$, $C_2^* = \frac{1}{M}\sum C_{2,n}$, $C_1^* = \frac{1}{M}\sum C_{1,n}$, and $C_0^* = \frac{1}{M}\sum C_{0,n}$.

Now, by varying A^{ref} or k_2 in a reasonable range (e.g., $A \in \left[\frac{v_s \times Peak_{Exp}}{2r_p \times N_{pass}}, 20\right]$, $k_2 \in [0.1, 12]$), a set of possible (A^{ref}, k_2) pairs can be obtained. However, the set remains too large to efficiently search for the corresponding $DE(\alpha)$. To refine the set of possible (A^{ref}, k_2) values, we evaluate some other points located at $x > 0$, and then compute their deposition heights without considering the effect of impact angle. Since $DE(\alpha)$ is less than one at these points, if the computed deposition height does not exceed the experimental value, the corresponding (A^{ref}, k_2) pair can be excluded from the solution domain. Fig. 4 outlines the overall algorithm used for extracting empirical constants, including this initial refinement step.

After the first refinement, the solution space for (A^{ref}, k_2) becomes significantly constrained. At this stage, it is computationally feasible to evaluate each remaining pair and identify the corresponding $DE(\alpha)$. To do so, an iterative algorithm has been developed that tracks the impact angle and adjusts its associated DE for selected points at $x > 0$. The algorithm begins by generating a random set of $DE(\alpha)$ values between 0 and 1 using MATLAB's built-in random number function. Because this initialization is entirely random, each execution of the code, even with identical inputs, produces a different set of $DE(\alpha)$ initial values. These values are subsequently reordered in descending order to ensure consistency with the physical behavior observed during spraying. When the nozzle is initially perpendicular to the substrate, the impact angle is close to zero and DE is high; as the deposit grows and the local surface slope increases, the impact angle rises, and DE progressively decreases in subsequent passes. Although the initialization introduces randomness, its influence on the final solution is negligible because the optimization routine systematically converges toward a unique $DE(\alpha)$ distribution with minimal dispersion for the corresponding α values. This procedure preserves both the expected physical trend and the stability of the final solution. Afterward, the numerical growth at the selected points,

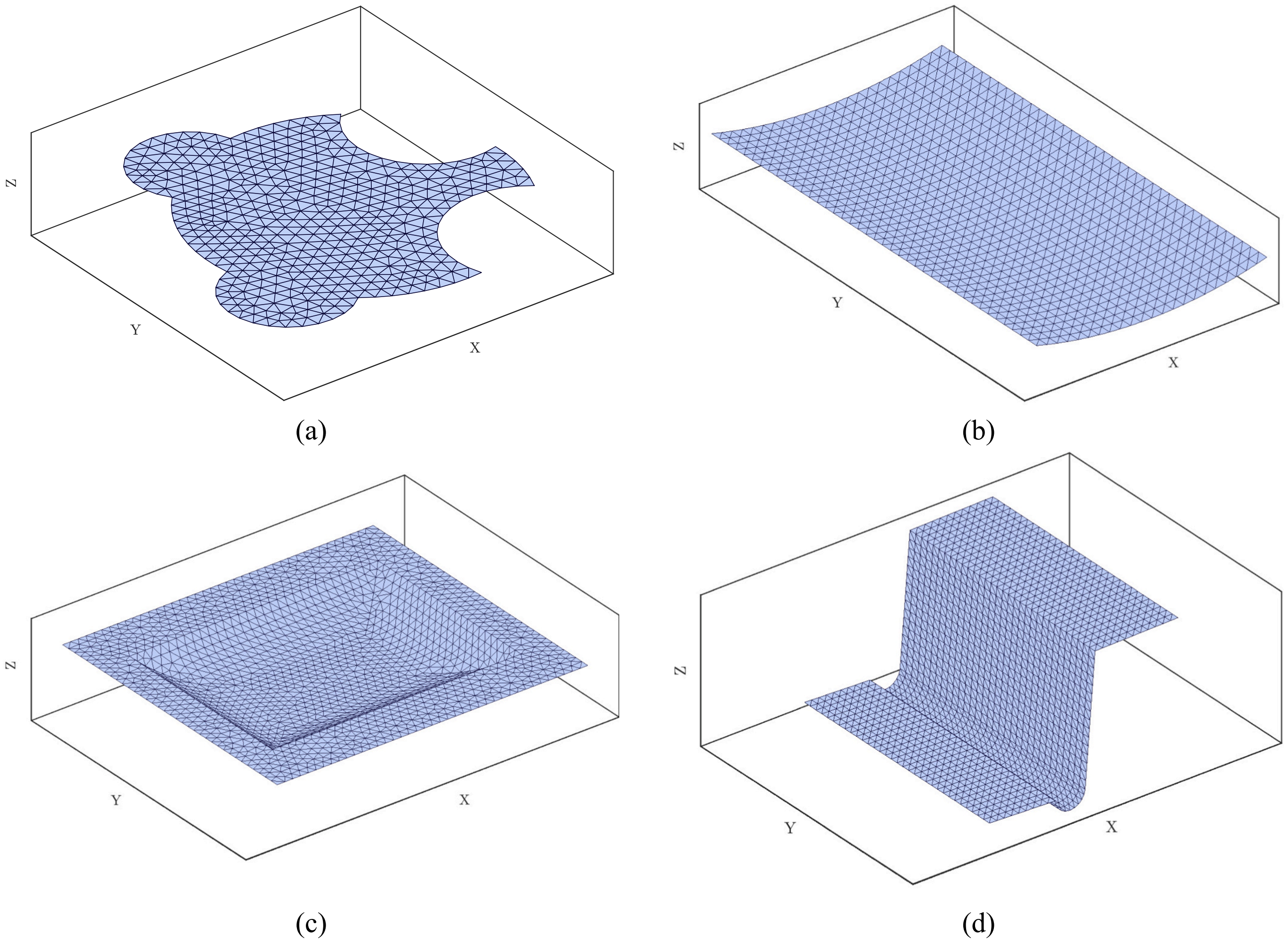

Fig. 5. Examples of substrate surfaces imported into the code, demonstrating varying levels of complexity: (a) a non-convex flat substrate, (b) a curved substrate, (c) a dented substrate, and (d) the substrate used to validate the new shadow effect algorithm.

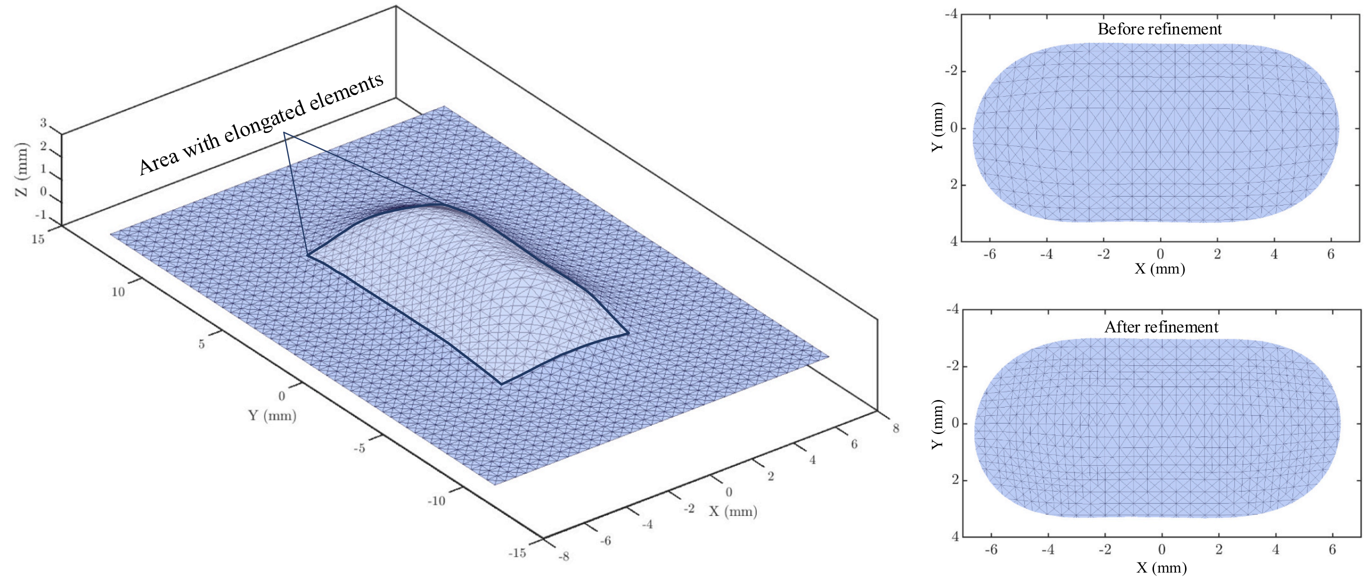

Fig. 6. An example demonstrating the performance of mesh refinement subroutine.

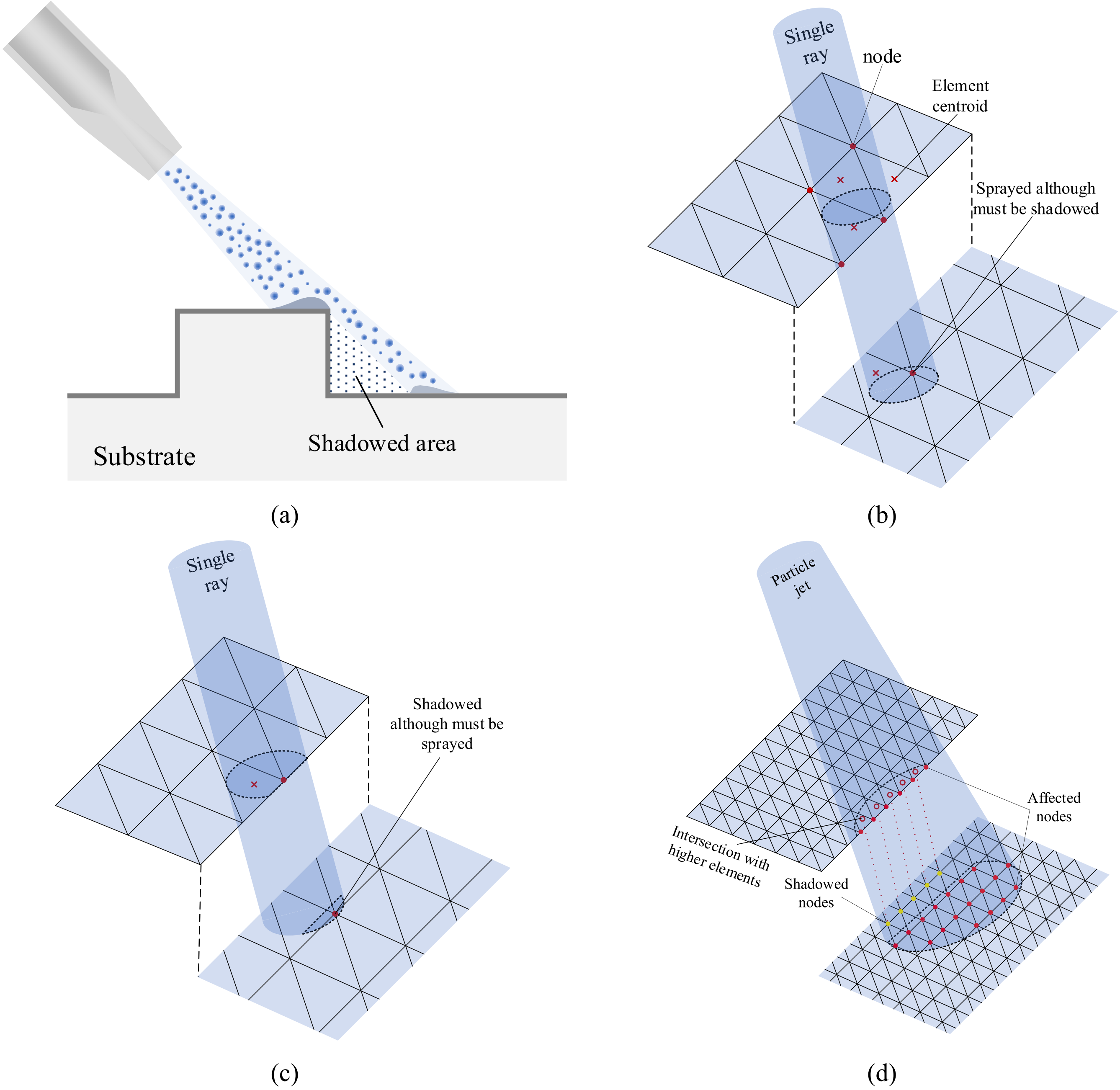

Fig. 7. (a) Schematic representation of the shadow effect. Potential issues with the ray-scanning scheme: (b) A false positive detection caused by misalignment of the mesh at different heights, and (c) a false negative detection due to an insufficient number of rays. (d) Illustration of the new shadowing scheme.

calculated using the current $DE(\alpha)$, is compared with experimental measurements. Based on the differences between them, the $DE(\alpha)$ values are iteratively adjusted to minimize the error.

Once the numerical prediction at the selected points matches the experimental deposition profile, the dispersion in the resulting $DE(\alpha)$ distribution is calculated. Physics dictates that similar impact angles should result in the same DE. Hence, the optimal $\left(A^{ref}, k_2\right)$ pair would be the one that yields the least dispersion in $DE(\alpha)$.

Finally, a second refinement is performed by comparing the experimental and numerical peak heights of the track profile. This step corrects the values of A^{ref} and k_2, as the initial assumption, i.e., the point located at $x = 0$ is entirely unaffected by $DE(\alpha)$, introduces small errors and leads to an underestimation of these parameters.

To quantify the dispersion index, the distribution of $DE(\alpha)$ is partitioned into intervals of four degrees, and the standard deviation within each interval is computed. The mean value of these standard deviations across all intervals is then defined as the dispersion index.

Moreover, an early stopping criterion is implemented in the code to avoid checking all possible $\left(A^{ref}, k_2\right)$ pairs. If the dispersion index increases for ten consecutive pairs, the program stops and returns the pair producing the lowest dispersion index. Once the empirical constants are determined, the second phase of the developed framework focuses on solving Eq. (5) for an arbitrary spraying process.

3.2. Phase II: deposit growth simulation

In this section, we present the 3D mesh-based model capable of simulating the deposit growth with full flexibility in substrate geometry, nozzle trajectory, and nozzle speed.

Eq. (5) constitutes an initial-boundary value problem defined over

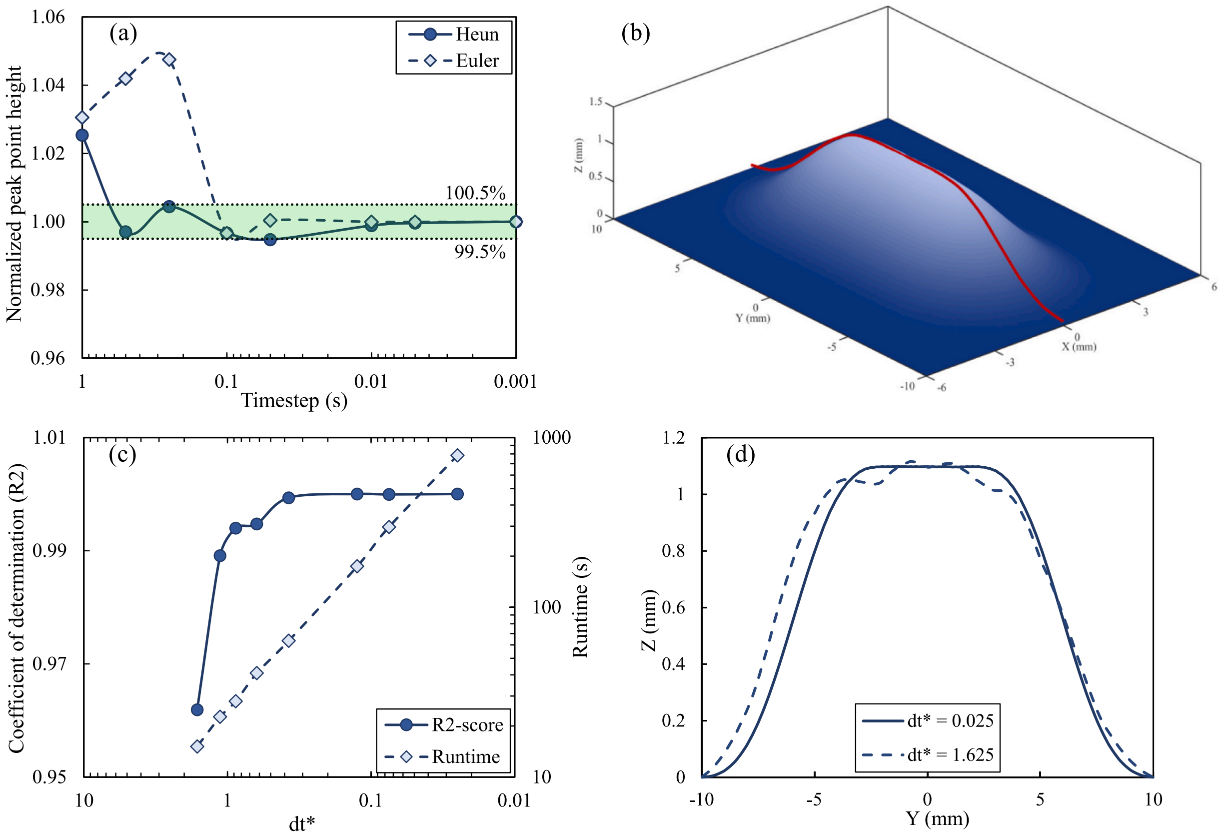

Fig. 8. (a) Timestep sensitivity analysis for a stagnant nozzle (one-spot spraying) using the Heun method and the first-order Euler method. (b) Cross-section curve representation used to control the smoothness of the deposition profile during continuous spraying. (c) Coefficient of determination (R^2-score) calculated between the reference deposition curve ($dt^* = 0.025$) and curves obtained using various values of dt^* for a 4-pass deposition. (d) Comparison of the final deposition cross-section profiles at $x = 0$ for $dt^* = 0.025$ and 1.625.

both spatial and temporal domains, for which the finite element method provides a robust and systematic numerical solution. Here, we present the developed code to solve Eq. (5) and its key features. We begin by describing the spatial discretization, followed by the concept of the shadow effect and the newly developed algorithm to simulate it. Next, we outline the code's flexibility in defining various toolpaths and nozzle orientations. Finally, we describe the explicit method used for temporal discretization and solving the PDE.

3.2.1. *Spatial discretization*

The substrate surface is provided as an input to the developed program in the form of a stereolithography (STL) file, which is discretized using bi-linear triangular elements (triangles with three vertices). Each STL file contains two matrices: one for the nodal coordinates and another for the element connectivity, which defines the number of nodes per element. The meshing procedure can be performed using any commercial software, such as Abaqus, that supports STL file export. Fig. 5 illustrates some examples of substrates with various levels of complexity (non-convex, curved, dented and prone to shadow effect) that can be processed by the code.

A mesh refinement subroutine has also been embedded in the code to keep the size of the elements within a reasonable range during the simulation. In this function, an element is refined when one of its edge lengths surpasses a pre-defined threshold (see Fig. 6). The mesh refinement process can be configured to run at specified increments such as every n simulation steps to optimize computational efficiency.

3.2.2. *Shadow effect*

The concept of shadow effect was first introduced by Wu et al. [19], highlighting that certain convex features on the substrate can obstruct particle flight, thereby preventing deposition on lower surfaces as depicted in Fig. 7a. While the conceptual basis of the shadow effect is relatively straightforward, its practical implementation presents considerable challenges. Wu et al. [19] proposed a ray-scanning strategy in which multiple rays (modeled as very narrow cylinders) radiate from the nozzle to determine whether a surface region is obstructed by another part. Vanerio et al. [23] adopted the same approach, excluding elements located farther from the nozzle from deposition if closer elements block the particle path.

However, this strategy has certain limitations, leading to inaccuracies in identifying shadowed elements. These limitations, as shown in Fig. 7, include: i) when modeling the particle jet as a divergent truncated cone, the density of rays decreases as SoD increases. This can result in missed shadowed elements if they do not intersect with a ray, reducing the accuracy of shadow detection. ii) elements at different heights must be properly aligned for the ray-scanning scheme to identify them correctly. Should a ray intersect a lower element but fail to identify a node or element centroid on the upper surface, owing to its trajectory passing between such features, the method will overlook the shadowed node or element (as illustrated in Fig. 7b) and iii) the user must define the number of rays based on the mesh size. This dependency prevents the use of different mesh sizes or free mesh generation schemes, restricting the ability to handle complex geometries (Fig. 7c).

To address the aforementioned limitations, the present model incorporates a novel methodology for shadow detection. In this method, a line is projected upward from each affected node in a direction parallel to the spray stream boundaries, converging toward the nozzle axis. If the projected line intersects an element positioned at a higher elevation, i.e., with a greater Z-coordinate, then the node in question is classified as shadowed. Otherwise, if no such intersection occurs, the node is

Table 2

Specifications of experimental tests used to validate the developed framework.

Sample	Powder material	Nozzle speed $(\frac{mm}{s})$	SoD (mm)	Spraying angle	# Passes	# Tracks
1	Pure Cu	75	30[a]	0°	20	1
2				0°	14	
3				0°	10	
4				15°	14	
5				30°	14	
6				45°	14	
7				0°	14	2
8				0°	14	3
9	Ti6Al4V	250	30[b]	0°	40	1
10	[34]			0°	20	
11				0°	10	
12				10°	20	
13				20°	20	
14				30°	20	
15		150		0°	20	
16		350		0°	20	
Shadow effect		250		30°	20	

[a] SoD was preserved throughout the experiment, meaning the nozzle height increased after each pass. The same condition has been applied in the simulations.

[b] Nozzle height position remained constant throughout the experiment. The same condition has been applied in the simulations.

considered exposed and eligible for deposition.

Fig. 7d illustrates the schematic of the new shadowing algorithm: red dots denote affected nodes, while yellow dots indicate shadowed nodes, even though they lie within the nominal particle jet. These nodes are blocked because their projected lines intersect with higher elements, thus preventing deposition.

The new shadowing algorithm not only overcomes the limitations of the previous scheme but also operates independently of user input, mesh size, and alignment, making it fully automated. The routine developed for identifying sprayed nodes also returns r, r_P, and SoD for each affected node.

3.2.3. Toolpath design and impact angle calculation

After developing the subroutines for mesh refinement and shadow effect detection at a given nozzle position, the next step is to enable the code to interpret nozzle trajectories during the simulation and compute the impact angle for each affected node. This is achieved through a subroutine that divides the toolpath into n user-defined increments, based on the nozzle's start and end positions and orientations. The subroutine generates a matrix containing the nozzle's position and direction at each increment. If the nozzle direction changes between the start and end points, the code performs a linear interpolation to determine the direction at intermediate positions. The current version imposes no restrictions on nozzle motion or orientation. Moreover, the subroutine can approximate circular movements by decomposing them into multiple linear segments.

Furthermore, a subroutine is required to calculate the surface normal at each node. This is accomplished by fitting a plane to the nodes located within a specified distance from the affected node and computing the corresponding normal vector. This non-local approach reduces numerical noise and helps preserve the smoothness of the evolving deposition profile. Computed normal vectors, together with the nozzle direction, are used to determine the local impact angle at each node. Importantly, in the current implementation, deposition growth is modeled along the surface normal, unlike previous implementations which assumed growth along the nozzle direction [23,24]; this feature makes the new model more realistic. The normal vector calculation subroutine is executed after each increment or mesh refinement to update the normal of existing elements or compute them for newly generated ones.

3.2.4. The PDE solver

By defining the particle jet through the simulation, the boundary conditions in Eq. (5) are considered implicit. Hence, it needs to be solved in the temporal domain. The Heun method [33], also known as the modified Euler method, was employed to solve the PDE explicitly. Using this approach, the growth of each node is determined based on the duration for which it is exposed to the particle jet, with these temporal intervals computed based on the nozzle transverse speed and the total path length of the tool trajectory.

Euler–Heun is a second-order predictor-corrector method that averages the slopes at the beginning and end of the interval $[t_n, t_n + h]$, where h represents the time step. This method has second-order accuracy, meaning that if the time step is halved, the error decreases by a factor of four [33]. It can be expressed as:

$$Z_{n_s+1} = Z_{n_s} + \frac{h}{2}\left(Z'(\overline{Z_{n_s+1}}, t_{n+1}) + Z'(Z_{n_s}, t_n)\right) \tag{11}$$

where

$$\overline{Z_{n_s+1}} = Z_{n_s} + hZ'(Z_{n_s}, t_n) \tag{12}$$

This method significantly enhances computational efficiency. In contrast, the first-order Euler method requires the use of significantly smaller timesteps between successive nozzle positions to maintain a comparable level of accuracy. On the other hand, the Heun method allows for larger timesteps while maintaining a precise representation of the temporal intervals during which the nozzle remains at each position. To ensure numerical stability and timestep independence in the simulations, a detailed timestep sensitivity analysis was conducted, as shown in Fig. 8. Two aspects were investigated: (i) the convergence behavior for a stationary nozzle and (ii) the surface smoothness for a continuously moving nozzle. For the stationary case, a single-spot deposition on a flat substrate was simulated to determine the minimum timestep required for convergence of the deposition peak height. As illustrated in Fig. 8a, the first-order Euler method required a timestep smaller than 0.1 s to reach convergence, whereas the Heun method achieved comparable accuracy with a larger timestep of 0.5 s, confirming its superior numerical efficiency and robustness.

For the moving nozzle case, the smoothness of the final deposition shape was evaluated by defining a dimensionless timestep parameter,

$$dt^* = \frac{timestep \times v_s}{D_N} \tag{13}$$

where D_N stands for nozzle diameter. Analyses performed for a four-pass deposition ($v_s = 75\ mm/s$, $D_N = 6\ mm$) demonstrated that both the PDE solver timestep and nozzle motion parameters significantly influence the resulting shape. The final deposition profiles along $x = 0$ were compared (see Fig. 8b). A quantitative comparison using the coefficient of determination (R^2) between the reference curve ($dt^* = 0.025$) and those obtained with larger timesteps (see Fig. 8c) indicated that $dt^* \leq 0.625$ ensures a sufficiently smooth and physically realistic deposition profile. The corresponding profiles for $dt^* = 0.025$ and $dt^* = 1.625$ are compared in Fig. 8d. This criterion was subsequently applied throughout the simulations to maintain both accuracy and computational efficiency.

The following are the key new features that distinguish the current framework from previous implementations:

- Extended flexibility in nozzle path and direction.
- The particle jet is modeled as a truncated divergent cone, providing a more realistic representation of the jet distribution.
- Deposition growth is calculated along the surface normal rather than the nozzle axis, offering a more physically accurate approach.

Table 3

Variations of A and k_2 as functions of the number of tracked points.

# Points	4	6	8	10	12	14	16
A (mm/s)	5.271	5.319	5.319	5.398	5.366	5.398	5.398
k_2	2.461	2.542	2.542	2.676	2.623	2.676	2.676

- A new shadowing algorithm is developed that operates independently of user input and is well-suited to the mesh-based nature of the code.
- An adaptive A value based on the SoD is introduced, enabling more accurate simulation of thick deposit formation.

4. Results and discussion

This section presents a rigorous evaluation of the developed framework. First, a comprehensive parametric analysis is performed on the code used for extracting the empirical constants, aimed at demonstrating the robustness of the results obtained for varying conditions. Specifically, we examine the influence of the number of points and the number of passes on the resulting constants for the same material and process parameters. Second, the constants obtained in the first phase are used as input for the second one, to simulate the deposition growth under various spraying conditions. The simulated deposition profiles are then compared with experimental data to validate the accuracy of the integrated framework. Two different materials, copper and a titanium alloy (Ti6Al4V), were used to evaluate the proposed method. A high-

Table 4

A and k_2 as functions of the number of passes.

# Passes	10	14	20
A (mm/s)	5.3386	5.0728	5.3984
k_2	2.6051	2.568	2.6764

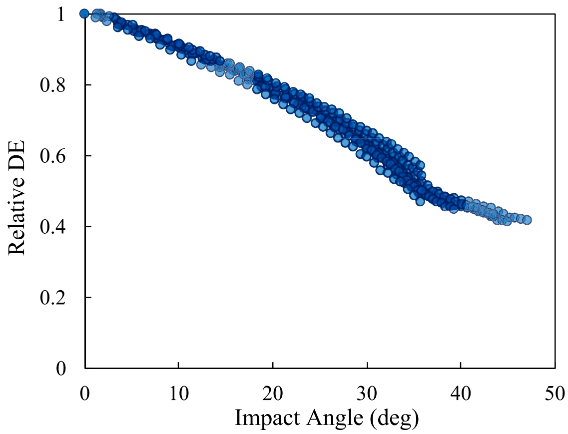

Fig. 10. $DE(\alpha)$ distribution for Ti6Al4V obtained from sample 9 and tracking 10 points.

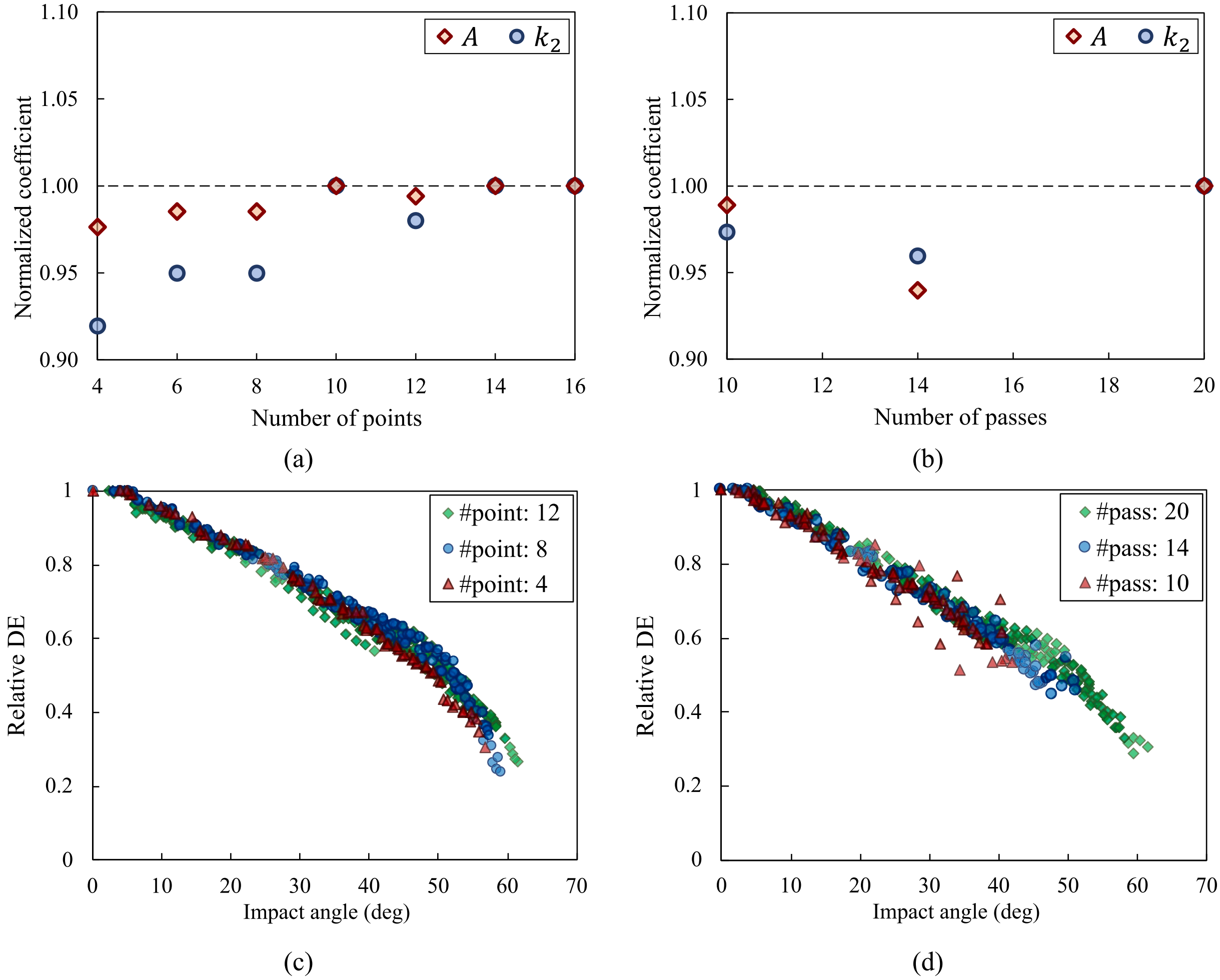

(a)

(b)

(c)

(d)

Fig. 9. Results of the parametric analyses: variation of A and k_2 with respect to (a) the number of tracked points and (b) pass number; variation of $DE(\alpha)$ with respect to (c) the number of tracked points and (d) pass number.

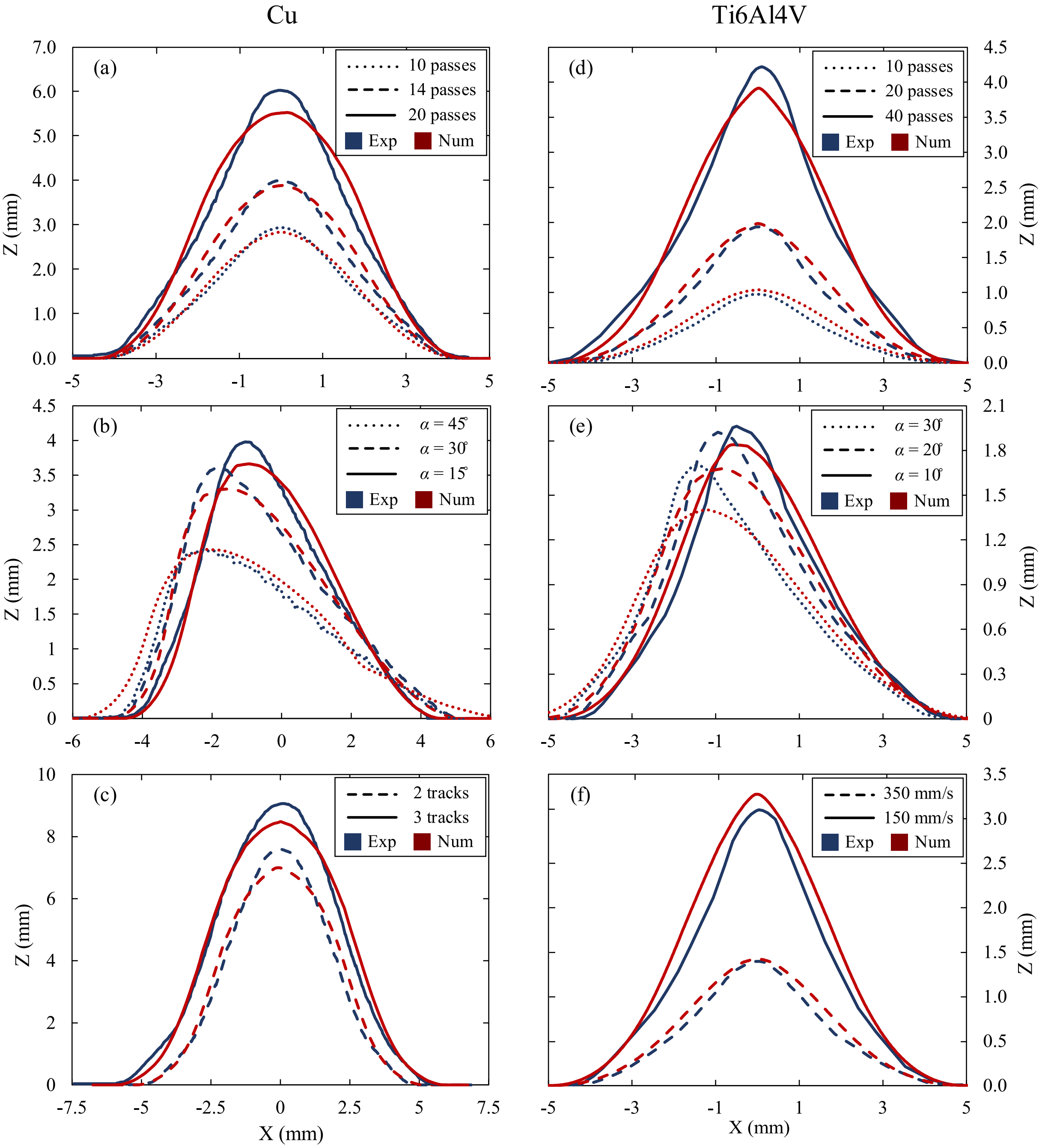

Fig. 11. Comparison between the experimental and numerical deposition profiles for (a–c) copper and (d–f) Ti6Al4V deposits. Experimental data for Ti6Al4V were extracted from [34].

pressure 6/11 cold spray system (Impact Innovations GmbH, Germany) was employed to deposit the powders using nitrogen as the carrier gas. Copper particles were sprayed onto copper substrates at a gas temperature of 750 °C and a pressure of 40 bar. For Ti6Al4V, the spraying was performed at a gas temperature of 1100 °C and a pressure of 50 bar. Table 2 reports the specifications of the experiments used to validate the codes. For each material, the experimental profile described in the first row was used to extract the empirical constants, i.e., samples 1 and 9.

4.1. Parametric analysis

This section evaluates the robustness of the code developed to extract the parameters A, k_2, and $DE(\alpha)$ of the analytical model. A robust implementation should produce consistent values for these constants regardless of the variations in the number of tracked points (as illustrated in Fig. 2) or the use of different experimental datasets for the same material and process parameters. To assess this robustness, first, the experimental deposition profile of sample 1 was analyzed by systematically increasing the number of tracked points from 4 to 16, with the corresponding constants recorded. In all analyses, only half of the deposition profile has been considered, from $x = 0$ to $x = r_P$, due to symmetry. The results for A and k_2 regarding the number of tracked points are presented in Table 3.

The values normalized with respect to the results obtained for 16 tracked points are shown in Fig. 9a. The results indicate that even with only 4 tracked points, A and k_2 reach over 97% and 92% of their respective converged values. It is worth noting that, due to the non-smooth nature of the experimental deposition profile and the shifting

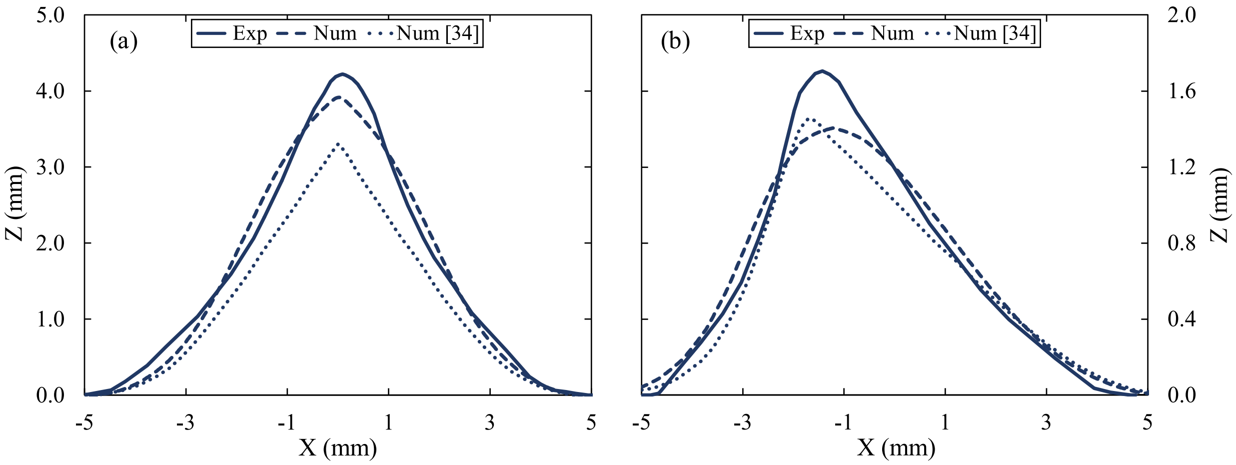

Fig. 12. Comparison between the numerical predictions of this study and the previous model [34] against experimental data for (a) a 40-pass perpendicular spray and (b) a 20-pass spray at a 30° inclination. The experimental profiles were extracted from [34].

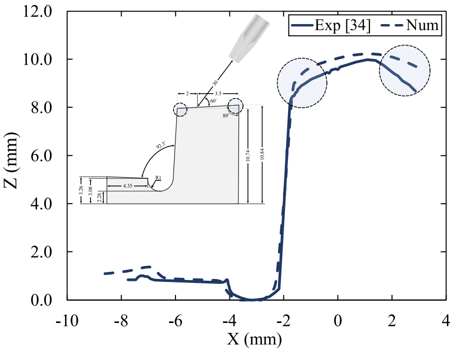

Fig. 13. Evaluating the performance of the model to predict shadow effect: comparison between the simulated results and the experimental profile (all units in the substrate schematic are in mm).

position of the tracked points across different cases, slight variations in the results are expected, such as the deviation observed in the 12-point case in Fig. 9a. Nonetheless, the results show that tracking more than 8 points ensures the convergence of the results.

Additionally, the empirical constants should remain consistent when using experimental tests with a different number of passes, used as a reference for the numerical calculations. To examine this, samples 1, 2, and 3 from the Cu dataset were analyzed, as summarized in Table 4. The normalized values A and k_2 with respect to those obtained for 20 passes are also depicted in Fig. 9b. When varying the number of passes, additional experimental uncertainties are introduced. However, the induced variations remain within an acceptable range. Moreover, although only slightly, the effect of the number of passes is not accounted for in the model. This is because increasing the number of passes can alter the thermal conditions of the process, thereby affecting the DE during higher pass counts.

The computed $DE(\alpha)$ distributions for different numbers of tracked points and passes are presented in Fig. 9c and d, respectively. The $DE(\alpha)$ distribution exhibits reasonable dispersion, with greater variability observed when varying the number of passes. The present numerical framework calculates the DE at significantly small increments of impact angles, enabling an accurate fitting of the function. However, based on the highest impact angle of the possible applications, the thickness of the experimentally obtained deposit that is used to derive $DE(\alpha)$ should be sufficiently high such that it contains data regarding those impact angles. This is obvious in Fig. 9d, as using a 10-pass deposition shape gives the DE values for only impact angles up to 40°, while the 20-pass deposition contains data for up to 60°.

After confirming the robustness of the code, it was employed to extract the empirical constants from Sample 9 for Ti6Al4V, yielding $A = 6.333\,mm/s$ and $k_2 = 3.941$. The corresponding $DE(\alpha)$ distribution for Ti6Al4V is also shown in Fig. 10.

Once the empirical constants of Klinkov's model were obtained, their accuracy was evaluated by comparing the experimental and numerical deposition shapes, as detailed in the following section.

4.2. Comparison with experiments

To evaluate the accuracy of the integrated predictive framework, numerical and experimental deposition profiles are compared across different cases. It is important to emphasize that all empirical constants were derived from a single experimental test for each material.

Fig. 11a–c present a comparison between the experimental and predicted deposition profiles for pure copper (Samples 1–8 in Table 2), while Fig. 11d–f show the corresponding results for Ti6Al4V. As observed, the simulated deposition profiles show strong agreement with the experimental data, confirming the accuracy of the derived empirical constants and the reliability of the simulation code. It is worth noting that, in the case of multiple tracks (Fig. 11c), the hatch distance between adjacent tracks is 1.5 mm, and each deposition pass is applied to two or three consecutive tracks.

One area where discrepancies were observed is near the peak of the deposition profile, with these deviations becoming more pronounced as the deposition thickness increases. Several factors may explain this behavior. First, the assumed deposition shape function $J(r, r_P)$ may not accurately capture the true deposition profile. Thus, as the thickness increases, the associated errors tend to accumulate. Another contributing factor is the variation in thermal conditions during deposition. In thicker coatings, the nozzle dwell time over the surface increases, leading to a gradual rise in the temperature of both the substrate and the previously deposited layers. This temperature increase may soften the material and enhance the DE. This explanation is plausible, as the simulations generally tend to underestimate the deposition height in thicker cases.

Moreover, the effects of the nozzle speed are considered to be linear in the current framework, as also reported in [16,35]. This may hold for relatively small variations in nozzle speed, as in the case of the reference experimental test. However, for larger changes, thermal conditions can significantly influence deposition behavior, resulting in discrepancies between experiments and numerical predictions (Fig. 11f).

To further investigate the accuracy of computed constants, the results were also compared with a previous model developed in our group

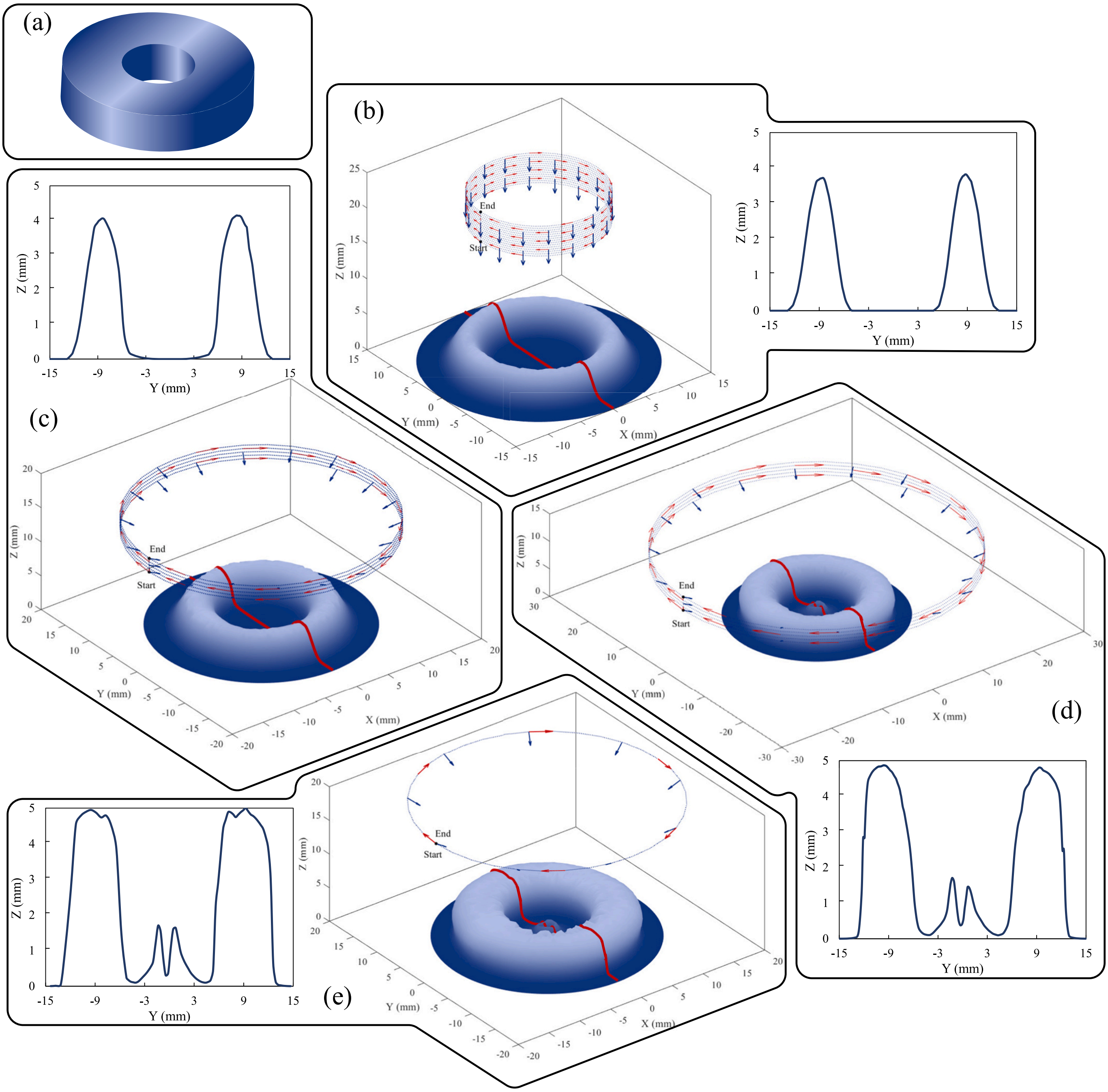

Fig. 14. (a) Schematic representation of the circular ring target geometry. Sequential stages of cold spraying with corresponding cross-sectional profiles: (b) perpendicular spraying for 15 passes, (c) inside-wall compensation with 5 passes at 50°, (d) outside-wall compensation with 5 passes at 50°, and (e) crown compensation with 2 passes at 50°. (For interpretation of the references to colour in this figure, the reader is referred to the web version of this article.)

[23]. The comparison revealed that, for thin deposition layers, typical in coating applications, both models accurately capture the deposition geometry. However, in more complex scenarios, such as thick depositions or high-angle spraying, common in AM or repair applications, the current model provides more accurate predictions of the deposition shape. As shown in Fig. 12a, the previous method deviates from the expected Gaussian-like profile, producing a triangular shape as the number of layers goes up to 40. This may stem from the fact that the $DE(\alpha)$, used in the previous study [23] was obtained by fitting a curve to a few data points at discrete impact angles, which may have reduced its accuracy. A similar trend in overall shape prediction is observed in Fig. 12b, although both models exhibit comparable errors near the peak of the experimental profile.

Finally, the performance of the new shadowing algorithm is evaluated against the experimental deposit shape presented in [23]. As shown in Fig. 13, the proposed algorithm accurately identifies the shadowed regions. An important observation concerns the regions near the edges of the substrate, as highlighted by the dashed circles in Fig. 13. In these areas, relatively large discrepancies are observed between the simulated and experimental results. This phenomenon, referred to as the "*edge effect*", leads to reduced DE near the substrate boundaries, resulting in inclined deposition profiles at the edges. The edge effect has also been reported in a previous study [36]. Nevertheless, the current model is not capable of capturing this effect. The edge effect can be significant in AM and repair applications, where it may be necessary to design compensating passes. Thus, modifying the analytical and numerical models such

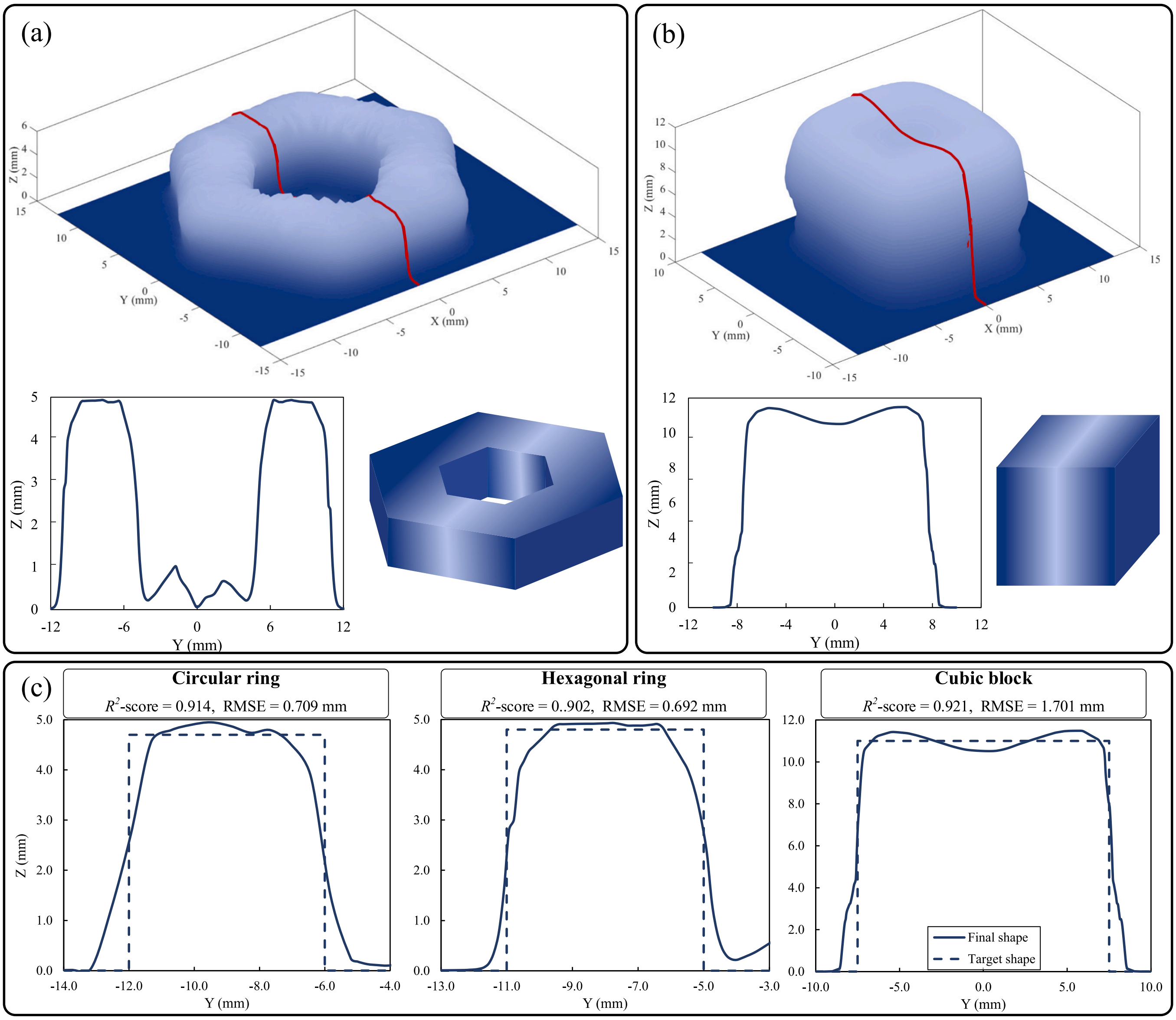

Fig. 15. Final deposition shapes of the modeled demonstrators with schematic representations of the target geometries: (a) hexagonal ring and (b) cubic block. (c) Quantitative comparison between target and simulated profiles (due to symmetry, only one side of the cross-sections was compared for circular and hexagonal rings).

that they can capture the effects of substrate boundaries on the deposition shape could be a valuable direction for future improvement.

4.3. Toward toolpath planning for shape control

One key objective of the predictive models for deposition shape is to minimize trial-and-error experiments in achieving the desired final geometry by optimizing toolpath strategies. This becomes particularly critical in applications requiring thicker deposits, such as AM and repair. In this subsection, we highlight this capability of the developed deposition growth simulation model. Owing to its efficiency and versatility, the model allows visualization of dozens of simulations with varying toolpath strategies (e.g., linear and circular paths with different nozzle angles) within only a few hours. To illustrate this, three representative geometries were considered: a cubic block, a circular ring, and a hexagonal ring.

Simulations were performed using copper spraying parameters. As it is well established, simple perpendicular multi-pass spraying results in thicker deposits near the substrate and thinner ones toward the top. To mitigate this effect, compensation passes, typically achieved through angled spraying along the peripheral walls, are necessary to obtain a more uniform thickness along the build direction. Fig. 14 illustrates the schematic and deposition sequence for a circular ring, including both the primary spraying and the recompensation passes. In Fig. 14, nozzle paths are highlighted with blue dotted lines and red arrows, while spraying directions are indicated by blue arrows. It was observed that, following compensation of the outer wall, an outgrowth formed at the center of the substrate, which can either be removed through suitable post-processing or avoided by adopting alternative spraying strategies.

A similar simulation was conducted for the hexagonal ring, whereas for the cubic block, five parallel tracks with a hatch spacing of 2 mm were deposited for 20 passes, followed by 12 compensation passes using inclined spraying at 50°, as shown in Fig. 15a and b. It should be emphasized that the toolpaths employed in these examples were not optimized but were used solely to demonstrate the capability of the code in picturing the spraying process and reproducing realistic phenomena, such as the formation of outgrowths in circular and hexagonal rings after outside-wall recompensation. Still, a comparison between the desired target profiles and the simulation results is presented in Fig. 15c. For each case study, both the root mean square error (RMSE) and the coefficient of determination (R^2-score) are provided. It should be noted that, due to symmetry, only half of the cross-sections were considered for the circular and hexagonal ring cases. As shown in Fig. 15c, although the toolpaths were not fully optimized, the similarity between the simulated and target profiles exceeds 90%. The corresponding simulation videos, presented at 0.5× speed for improved clarity, are provided in the Supplementary materials (Videos S1–S10).

5. Conclusions

This study proposes a two-phase computational framework for efficient shape prediction in the cold spray deposition process, aimed at improving accuracy and reducing the experimental burden. The first phase develops a systematic numerical model to extract key empirical parameters, including impact angle-dependent deposition efficiency, from a single experimental profile. The second phase integrates these parameters into a mesh-based simulation tool featuring also a new, mesh-independent shadowing algorithm for enhanced accuracy when predicting complex geometries.

The framework was validated extensively against experimental data for copper and Ti alloy Ti6Al4V deposits, demonstrating strong agreement and improved fidelity over existing methods, particularly for thick and high-angle depositions. The significance of this model lies in its unique capacity to substantially reduce experimental reliance (requiring only one track) while concurrently achieving high accuracy. This capability, demonstrated through case studies on cubic, circular, and hexagonal geometries, establishes the simulator as a robust tool for toolpath optimization and achieving dimensional control in thick deposits.

While the current framework provides excellent predictive quality, its scope has identified specific limitations that direct future research. The discrepancies observed near the peak of thick deposits and at substrate edges indicate that the present model does not incorporate thermal effects (in-situ heating) or edge effects. Therefore, a key future objective is to couple the model with a thermal module to capture the influence of in-situ heating on deposition shape during prolonged spraying, which may lead to material softening and enhanced deposition. In parallel, future efforts should explicitly address edge effects to represent the reduced deposition efficiency near substrate boundaries. These developments will ultimately enable the automation of toolpath optimization through a real-time decision-making system, where predictive deposition modeling guides adaptive nozzle movements toward fully controlled cold spray additive manufacturing.

CRediT authorship contribution statement

Mohammad Reza Mehraban: Writing – original draft, Visualization, Validation, Methodology, Investigation, Formal analysis, Data curation, Conceptualization. **Mario Guagliano:** Writing – review & editing, Validation, Supervision, Resources. **Sara Bagherifard:** Writing – review & editing, Validation, Supervision, Funding acquisition, Conceptualization.

Declaration of competing interest

The authors declare that they have no known competing financial interests or personal relationships that could have appeared to influence the work reported in this paper.

Acknowledgements

This project has received funding from the European Union's Horizon Europe research and innovation program under the Marie Skłodowska-Curie grant agreement No 101119988 (Re-Make). SB acknowledges ArcHIDep funding from the European Research Council (ERC) under grant agreement n. 101044228. The authors acknowledge Roberta Falco's contribution for providing experimental data regarding copper deposits. Views and opinions expressed are, however, those of the authors only and do not necessarily reflect those of the European Union or the European Research Council Executive Agency. Neither the European Union nor the granting authority can be held responsible for them.

Appendix A. Supplementary data

Supplementary data to this article can be found online at https://doi.org/10.1016/j.jmapro.2026.03.070.

References

[1] Bagherifard S, Kondas J, Monti S, Cizek J, Perego F, Kovarik O, et al. Tailoring cold spray additive manufacturing of steel 316 L for static and cyclic load-bearing applications. Mater Des 2021;203:109575. https://doi.org/10.1016/j.matdes.2021.109575.

[2] Yu HZ, Tuncer N, Feng Z, editors. Solid-state metal additive manufacturing. Wiley; 2024. https://doi.org/10.1002/9783527839353.

[3] Kumaravel M, Bagherifard S, Guagliano M. Advancements in deposition of high entropy alloys using cold spray technology. J Therm Spray Technol 2024;34:1–36. https://doi.org/10.1007/s11666-024-01879-0.

[4] Wicaksono RA, Ardeshiri Lordejani A, Bagherifard S. Current trends and future perspective for cold spray metal-ceramic composites. Adv Eng Mater 2024:2401657. https://doi.org/10.1002/adem.202401657.

[5] Su Y, Zhou M, Li W, Yang X, Shi Q, Xiong Y, et al. Microstructural evolution and mechanical behavior of TA5 titanium alloy joint in low-temperature friction stir welding with various cooling rates. Eng Fail Anal 2025;176:1–19. https://doi.org/10.1016/j.engfailanal.2025.109667.

[6] Su Y, Yang X, Meng T, Wu D, Xu R, Xu H, et al. Effect of linear friction welding process on microstructure evolution, mechanical properties and corrosion behavior of GH4169 superalloy. Chin J Aeronaut 2024;37:504–20. https://doi.org/10.1016/j.cja.2024.03.039.

[7] Dang M, Guo Z, Ma T, Yang X, Su Y, Li W, et al. Microstructure evolution and mechanical properties of a linear friction welded TC4-DT titanium alloy joint. Mater Today Commun 2025;46. https://doi.org/10.1016/j.mtcomm.2025.112684.

[8] Champagne V, Helfritch D. The unique abilities of cold spray deposition. Int Mater Rev 2016;61:437–55. https://doi.org/10.1080/09506608.2016.1194948.

[9] Assadi H, Kreye H, Gärtner F, Klassen T. Cold spraying – a materials perspective. Acta Mater 2016;116:382–407. https://doi.org/10.1016/j.actamat.2016.06.034.

[10] Tiamiyu AA. Solid-state cold spray welding: evaluation and future direction. J Adv Join Process 2023;8:100162. https://doi.org/10.1016/j.jajp.2023.100162.

[11] Yin S, Cavaliere P, Aldwell B, Jenkins R, Liao H, Li W, et al. Cold spray additive manufacturing and repair: fundamentals and applications. Addit Manuf 2018;21:628–50. https://doi.org/10.1016/j.addma.2018.04.017.

[12] Bagherifard S, Guagliano M. Fatigue performance of cold spray deposits: coating, repair and additive manufacturing cases. Int J Fatigue 2020;139:105744. https://doi.org/10.1016/j.ijfatigue.2020.105744.

[13] Falco R, Bagherifard S. Cold spray additive manufacturing: a review of shape control challenges and solutions. J Therm Spray Technol 2025;34:1023–41. https://doi.org/10.1007/s11666-025-01970-0.

[14] Wu H, Xie X, Liu M, Verdy C, Zhang Y, Liao H, et al. Stable layer-building strategy to enhance cold-spray-based additive manufacturing. Addit Manuf 2020;35. https://doi.org/10.1016/j.addma.2020.101356.

[15] Cai Z, Deng S, Liao H, Zeng C, Montavon G. The effect of spray distance and scanning step on the coating thickness uniformity in cold spray process. J Therm Spray Technol 2014;23:354–62. https://doi.org/10.1007/s11666-013-0002-0.

[16] Chen C, Xie Y, Verdy C, Liao H, Deng S. Modelling of coating thickness distribution and its application in offline programming software. Surf Coatings Technol 2017;318:315–25. https://doi.org/10.1016/j.surfcoat.2016.10.044.

[17] Yanjun Z, Wenbo L, Dayu L, Jinkun X, Chao Z. Modeling of thickness and profile uniformity of thermally sprayed coatings deposited on cylinders. J Therm Spray Technol 2018;27:288–95. https://doi.org/10.1007/s11666-017-0661-3.

[18] Zhang Y, Li W, Zhang C, Liao H, Zhang Y, Deng S. A spherical surface coating thickness model for a robotized thermal spray system. Robot Comput Integr Manuf 2019;59:297–304. https://doi.org/10.1016/j.rcim.2019.05.003.

[19] Wu H, Xie X, Liu M, Chen C, Liao H, Zhang Y, et al. A new approach to simulate coating thickness in cold spray. Surf Coat Technol 2020;382. https://doi.org/10.1016/j.surfcoat.2019.125151.

[20] Li W, Wu H, Sokore M, Raoelison RN, Liao H, Costil S, et al. General-purpose numerical deposition modeling methodology based on mesh geometry reconstruction strategy in cold spray additive manufacturing system. Surf Coat Technol 2023;464:129563. https://doi.org/10.1016/j.surfcoat.2023.129563.

[21] Klinkov SV, Kosarev VF, Ryashin NS, Shikalov VS. Influence of particle impact angle on formation of profile of single coating track during cold spraying. In: AIP conf. proc. vol. 2027. American Institute of Physics Inc.; 2018. https://doi.org/10.1063/1.5065085.

[22] Klinkov SV, Kosarev VF, Shikalov VS. Control of cold spray process by changing of nozzle setting angle. In: AIP conf. proc. vol. 2125. American Institute of Physics Inc.; 2019. https://doi.org/10.1063/1.5117382.

[23] Vanerio D, Kondas J, Guagliano M, Bagherifard S. 3D modelling of the deposit profile in cold spray additive manufacturing. J Manuf Process 2021;67:521–34. https://doi.org/10.1016/j.jmapro.2021.05.013.

[24] Ardeshiri Lordejani A, Romanenghi L, Pollastri A, Guagliano M, Bagherifard S. Deposit shape control for local repair and welding by cold spray. J Manuf Process 2024;112:45–59. https://doi.org/10.1016/j.jmapro.2024.01.023.

[25] Xing C, Li W, Xu Y, Huang C. A novel three-dimensional profile prediction method integrated with particle acceleration simulation and layer stacking in cold spray additive manufacturing. Addit Manuf 2025;109:104866. https://doi.org/10.1016/j.addma.2025.104866.

[26] Ikeuchi D, Vargas-Uscategui A, Wu X, King PC. Neural network modelling of track profile in cold spray additive manufacturing. Materials (Basel) 2019;12. https://doi.org/10.3390/ma12172827.

[27] Liu M, Wu H, Yu Z, Liao H, Deng S. Description and prediction of multi-layer profile in cold spray using artificial neural networks. J Therm Spray Technol 2021;30:1453–63. https://doi.org/10.1007/s11666-021-01212-z.

[28] Savangouder RV, Patra JC, Palanisamy S. A machine learning technique for prediction of cold spray additive manufacturing input process parameters to achieve a desired spray deposit profile. IEEE Trans Ind Informatics 2024;20:1–9. https://doi.org/10.1109/tii.2024.3417300.

[29] Falco R, Jalayer M, Bagherifard S. Enhanced geometrical control in cold spray additive manufacturing through deep neural network predictive models. Virtual Phys Prototyp 2025;20:1–19. https://doi.org/10.1080/17452759.2025.2472388.

[30] Ikeuchi D, Vargas-Uscategui A, Wu X, King PC. Data-efficient neural network for track profile modelling in cold spray additive manufacturing. Appl Sci 2021;11:1–12. https://doi.org/10.3390/app11041654.

[31] Yang Q, Yang S, Yu H, Wang H. Impact of Laval nozzle structure on the flow characteristics of supersonic gas-solid two-phase flow. Powder Technol 2024;439. https://doi.org/10.1016/j.powtec.2024.119657.

[32] Liu Y, Zhang J, Wei J, Liu X. Optimum structure of a Laval nozzle for an abrasive air jet based on nozzle pressure ratio. Powder Technol 2020;364:343–62. https://doi.org/10.1016/j.powtec.2020.01.086.

[33] Ascher UM, Petzold LR. Computer methods for ordinary differential equations and differential-algebraic equations. Philadelphia, PA: Society for Industrial and Applied Mathematics; 1998. https://doi.org/10.1137/1.9781611971392.

[34] Vanerio D. 3D simulation of cold spray deposit profile: towards digitalization of cold spray additive manufacturing. Politecnico di Milano; 2020. https://hdl.handle.net/10589/166496.

[35] Wong W, Rezaeian A, Irissou E, Legoux JG, Yue S. Cold spray characteristics of commercially pure Ti and Ti-6Al-4V. Adv Mater Res 2010;89–91:639–44. https://doi.org/10.4028/www.scientific.net/AMR.89-91.639.

[36] Vaz RF, Albaladejo-Fuentes V, Sanchez J, Ocaña U, Corral ZG, Canales H, et al. Metal knitting: a new strategy for cold gas spray additive manufacturing. Materials Basel 2022;15:1–17. https://doi.org/10.3390/ma15196785.